Avoiding imaging artifacts from resonant modes in metamaterial superlenses

Iman Aghanejad, Kenneth J. Chau, and Loïc Markley*
School of Engineering, University of British Columbia, Kelowna, BC, Canada

(Received 30 November 2018; revised manuscript received 28 June 2019; published 31 July 2019)

Superlenses are imaging components that can overcome the diffraction limit associated with conventional dielectric lenses. An ideal superlens is a flat infinite slab of homogeneous double-negative material with $\varepsilon = \mu = -1$ embedded in air, which achieves perfect imaging by restoring all the spatial frequency components of an object to the image plane. It has been shown that any deviation from these homogeneous material parameter values limits the resolution of the lens and introduces a surface mode resonance with fields that dominate the image. While material loss can suppress the resonant mode, loss also reduces spatial resolution. In this paper, we investigate resonant modes arising in metamaterial superlenses of infinite and finite extent and show how they cause imaging artifacts and reduce imaging fidelity. We choose a well-studied periodic structure consisting of an array of magnetodielectric cylinders for the lens medium under test. We demonstrate that the presence of these artifacts can lead to erroneous interpretation of the standard two-source resolution test for lenses. We show that artifacts can be mitigated by introducing point defects into the array, which move the resonant modes to higher spatial frequencies and, in the case of finite lenses, suppress their amplitudes through radiation losses. This strategy enables more robust and reliable subwavelength imaging performance, improves the spatial resolution of the metamaterial lens, and reduces the deleterious effects of material losses.

DOI: 10.1103/PhysRevB.100.035137

I. INTRODUCTION

The resolution of classic optical instruments is limited by Abbe's diffraction limit in which details of an object smaller than half the wavelength of operation become blurred at the image plane [1]. These subwavelength details have high transverse spatial-frequency components in the Fourier spectrum, are carried by evanescent waves from the object, and are lost before reaching the image plane. It has been shown that an infinitely long flat slab of homogeneous double-negative material with $\varepsilon = \mu = -1$ embedded in air can overcome the diffraction limit by restoring all propagating and evanescent components of the object to the image plane [2]. This perfect lens was first introduced by Veselago [3], who showed that an isotropic and homogeneous double-negative medium could sustain left-handed propagating plane waves with antiparallel phase and group velocities. As a result, a flat slab of this material can focus all the propagating components of an object by negatively refracting them at the two interfaces of the slab. The slab, which we will refer to as a Veselago lens, was later shown to amplify evanescent waves through the excitation of bound modes guided along the slab over the evanescent spectrum [4,5].

The bound modes of a Veselago lens arise from the symmetric and antisymmetric coupling of surface-plasmon polaritons guided along the two interfaces of the slab. In other words, the (uncoupled) surface mode of a single interface (which resonates when $\varepsilon = \mu = -1$) splits into two slab bound modes with resonance frequencies above and below the single-interface resonance frequency [6,7]. The Veselago lens always operates between these two bound mode frequencies, amplifying each incident evanescent component to perfectly compensate for its decay in air [5]. As a result, a Veselago lens has a unity transfer function for all transverse spatial frequencies when the object plane is separated from the image plane by twice the lens thickness [2,5].

When the constitutive parameters of an infinite homogeneous slab deviate from -1, however, the bound modes appear at the operating frequency [8]. These resonances correspond to poles in the slab transfer function [9] and degrade the imaging performance of the slab in two ways [10]. First, the transfer function starts to rapidly decay for spatial frequencies above the bound mode wave number, thereby establishing an upper spatial-frequency cutoff. Second, components of the object which have transverse spatial frequencies at or near the bound mode wave number are overamplified throughout the slab, which prevents image formation. These bound modes must be suppressed by adding material losses to the slab; however, these losses reduce the evanescent amplification and further limit the resolution of the lens [10]. Therefore, to achieve subdiffractive imaging resolution, the resonant modes must be suppressed while still maintaining a spatial frequency cutoff above the free-space cutoff.

While the absence of homogeneous double-negative materials in nature precludes realizing an ideal superlens, subwavelength-spaced sources have been resolved using lenses composed of arrays of resonant inclusions [11–13]. Among them are metamaterial structures which can sustain backward-wave Bloch modes in all directions of propagation and therefore mimic left-handed behavior over the propagating spectrum. The extraction of double-negative effective parameters for metamaterials has suggested that they might be viable candidates for Veselago superlensing across the electromagnetic frequency spectrum [14–16]; however, the effect of finite lens dimensions, periodicity, and heterogeneity

*loic.markley@ubc.ca

on evanescent wave amplification needs further study. Furthermore, resonant modes are not completely bound to a lens with finite lateral extent and the impact of edge scattering on imaging performance must also be determined.

In this paper, we investigate how resonant modes within infinite and finite negative-index metamaterial lenses can affect imaging fidelity, resolution, and robustness. We select a standard metamaterial design composed of an array of magnetodielectric (MD) inclusions [17–22]. This metamaterial has been shown to mimic the left-handed behavior of a Veselago medium below the free-space cutoff and has been reported to be capable of super-resolution imaging [23]. By choosing lossless materials with matched electric and magnetic properties, the MD array offers arguably the closest metamaterial approximation to a homogeneous Veselago superlens. It features a high degree of spatial symmetry and exhibits identical responses for TE and TM polarization. In this paper we consider two-dimensional arrays of MD cylinders for simplicity. We start our investigation by choosing idealized lossless material parameters (similar to previous works referenced) in order to isolate the effect of resonant modes on imaging and establish a baseline performance. Employing full-wave simulations to calculate the electromagnetic response of the MD arrays, we show that finite lenses support low spatial frequency modes that are easily excited by the evanescent components of the object. These modes have field patterns that extend into the image plane with intensities on the order of the field representing the object, producing artifacts that can overwhelm the fields of the true image. For example, we show that a regular array of MD cylinders can image a pair of illuminating point sources when symmetrically centered in front of the lens but not when that symmetry is broken. This fact casts doubts on the standard two-source resolution test used by the community to benchmark metamaterial superlensing and demonstrates the importance of accounting for resonant modes in metamaterial superlens design.

Material loss can dampen resonant modes and suppress imaging artifacts, but it comes at the expense of reduced spatial resolution (often precluding super-resolution). In this paper, we show that imaging improvements can be made to the MD cylinder array by introducing vacancy point defects that shift the resonant bound modes to higher spatial frequencies and direct the edge scattering laterally away from the image plane. Higher spatial frequency bound modes increase the lens cutoff (maximizing resolution) while lateral scattering circumvents overamplification and decreases the artifacts in the image. Using multiple point sources at various lateral positions and spacings, we show that the defected array lens generates images that have greater resolution and fidelity than those generated by the regular array lens. Furthermore, due to its higher spatial bandwidth, superlensing in the defected array lens is shown to be more robust to material losses.

The rest of the paper is organized as follows. In Sec. II, we study the behavior of backward bulk modes in the regular and defected MD cylinder array metamaterials and compare them with an ideal lossless and homogeneous Veselago medium. In Sec. III, we study the bound modes guided along infinite metamaterial slabs and compare them to the bound modes in Veselago lenses of identical thickness. In Sec. IV, we study the dominant resonant modes in finite metamaterial lenses and describe the effects of scattering from the edges. In Sec. V, we study and compare the imaging performance of lossless and lossy metamaterial MD lenses for various multisource configurations. The final section concludes the paper and summarizes our findings. All the numerical analyses presented in this paper were conducted using the finite-element solver from COMSOL MULTIPHYSICS [24]. The homogeneous medium and metamaterial structures presented are independent of TM and TE polarization; however, we chose TM polarization to illustrate the results (i.e., the magnetic field lies perpendicular to the plane of propagation). All fields are assumed to be time harmonic with an implicit $e^{-i\omega t}$ dependence.

II. BULK MODES IN TWO-DIMENSIONAL MAGNETODIELECTRIC METAMATERIALS

In order to analyze the complete imaging performance of a lens, we need to know its response to propagating and evanescent incident waves. In negative-index metamaterial lenses, homogenization methods have been used to show that effective bulk parameters of propagating backward-wave Bloch modes may provide a quasi-isotropic negative-index response [14,16,23]. Here we show that this bulk response is not sufficient to determine the evanescent response and that further investigation is required. In Sec. II A, we analyze the bulk modes in an ideal homogeneous double-negative medium and use the results as a baseline reference for analyzing negative-index metamaterials. The two-dimensional bulk modes within a uniform regular array of MD cylinders and a defected array (comprising a grid of MD cylinder monolayers) are studied in Secs. II B and II C, respectively.

A. Ideal homogeneous double-negative medium

Let us consider an ideal isotropic homogeneous double-negative medium with frequency-dispersive relative material parameters

$$\varepsilon(\omega) = 1 - \tfrac{2{\omega_o}^2}{\omega^2}, \tag{1}$$

$$\mu(\omega) = 1 - \tfrac{2{\omega_o}^2}{\omega^2}, \tag{2}$$

where both ε and μ are equal to -1 at the operating frequency ω_o (note that these equations must necessarily contain loss terms at low frequencies, but we consider the limit at which losses are negligible at the frequencies of interest). We will refer to this medium as the Veselago medium. We call the wave number and wavelength corresponding to this frequency $k_o = \omega_o/c$ and $\lambda_o = 2\pi/k_o$, respectively, where c is the speed of light in free space.

Here, we describe the bulk modes of the Veselago medium at ω_o in terms of real transverse wave-vector component k_x. For the propagating spectrum ($|k_x| < k_o$), the eigenmodes are left-handed plane waves propagating in the xz plane with a purely real longitudinal wave-vector component $k_z = -\sqrt{k_o^2 - k_x^2}$. As shown by the solid gray equifrequency contours (EFCs) in Fig. 1, the wave vectors trace out a circle with radius k_o over which group velocity points inward. The EFC of right-handed plane waves propagating in free space has the same circular shape but with positive longitudinal wave-vector components and an outward pointing group velocity. Therefore, propagating waves incident from free space

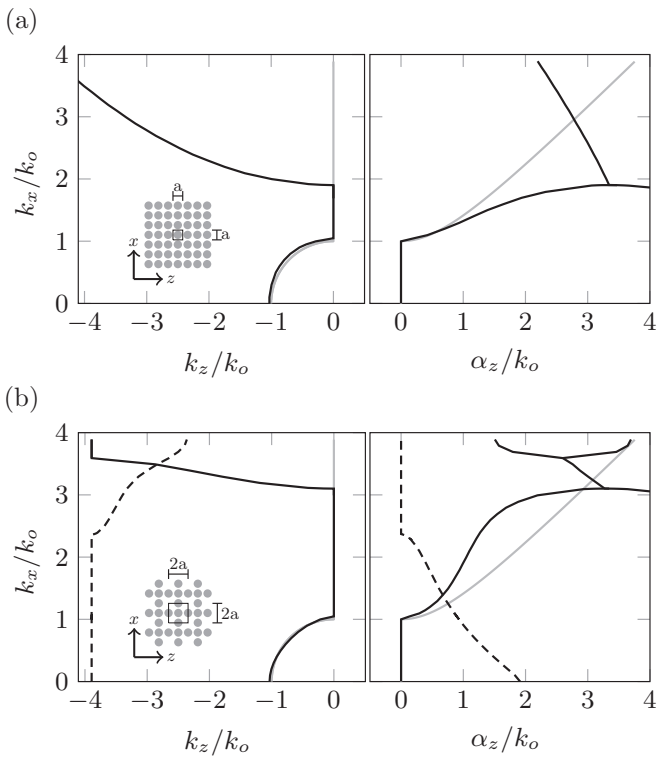

FIG. 1. The EFCs of the bulk eigenmodes at ω_o in (a) the regular array metamaterial (solid black lines) and (b) the defected array metamaterial (solid and dashed black lines), alongside the EFC of an ideal homogeneous double-negative medium (solid gray lines). In each plot, the complex longitudinal wave-vector components $k_z + i\alpha_z$ are plotted as a function of the real transverse wave-vector component k_x. Both diagrams are plotted over the first Brillouin zone of the defected array (i.e., up to the band edges at $|k_x| = \pi/2a = 3.89k_o$) in order to compare the salient features. The geometries of the defected and regular array metamaterials with their square unit cells are illustrated in the inset diagrams.

at any angle will be negatively refracted at the interface of the Veselago medium. Because of this property, a slab of this material can focus all propagating components of an object from a source plane to an image plane when the planes are separated by twice the lens thickness [3].

For the evanescent spectrum ($|k_x| > k_o$), however, bulk eigenmodes are evanescent waves in the z direction with a purely imaginary longitudinal component $i\alpha_z = i\sqrt{k_x^2 - k_o^2}$ which is identical to free space. Having similar evanescent modes as in free space with equal but opposite constitutive parameters satisfies a resonant condition at the interface between a Veselago half space and air for all values of k_x. These resonances correspond to surface-plasmon polaritons guided along the interface with a flat dispersion profile over the evanescent spectrum at ω_o. As will be further discussed in Sec. III A, these surface modes split into symmetric and antisymmetric coupled surface modes for an infinite flat slab of the Veselago medium. These bound modes provide the origins of evanescent wave amplification within the slab and consequently provide the mechanism for perfect imaging [4,5].

B. Regular array MD metamaterial

Here, we analyze the two-dimensional bulk modes in an infinite uniform regular array of magnetodielectric cylinders with $\varepsilon = \mu = 20$ which are embedded in air as the host medium [see the inset diagram in Fig. 1(a)]. The cylinders extend infinitely along the y axis with diameter $2r = 0.893a$, where a is the lattice constant of the array. The bulk modes are extracted at a fixed frequency by solving the wave equation over a unit cell for different transverse wave-vector components k_x [25].

As shown by the solid black line in Fig. 1(a), this periodic structure can sustain backward-wave Bloch modes for all directions of propagation. The circular EFC (traced by the fundamental Floquet wave vectors) mimics the homogeneous Veselago medium when the periodicity is equal to $a = 0.0646\lambda_o$, where once again λ_o is the free-space operating wavelength. Similar to the Veselago medium, a slab of this metamaterial can focus all the incident propagating waves from air through coupling with the backward-wave Bloch modes sustained within the slab.

As can be seen in Fig. 1(a), however, the dispersive behavior of the bulk modes deviates from the ideal Veselago medium over the evanescent spectrum, with the bulk modes taking on complex wave vectors at higher transverse spatial frequencies. This would naturally lead us to suspect that the slab bound modes also differ from those of the Veselago lens, potentially impacting the imaging performance of the MD metamaterial lens. In Sec. III B, we directly solve for the bound modes sustained in a slab of this metamaterial and analyze its response to an incident wave.

C. Defected array MD metamaterial

Here, we analyze the defected array metamaterial designed by introducing uniformly spaced vacancy point defects in the regular array MD metamaterial [see the inset diagram in Fig. 1(b)]. We can also view the defected array as a cross-hatched grid of MD cylinders made by vertical and horizontal MD cylinder monolayers which are spaced by distance $2a$ along the longitudinal (z) and transverse (x) directions, respectively. As shown by the solid black line in Fig. 1(b), the propagating backward-wave Bloch modes in the defected array can also mimic the circular EFC of the Veselago medium by adjusting the lattice constant to $2a = 0.1284\lambda_o$. Given the shape of the EFC, we expect that a slab of this structure focuses all incident propagating components through negative refraction (just like the regular MD array).

Although the dispersive behavior of dominant bulk modes in the regular and defected array metamaterials are very similar over the propagating spectrum, as shown by the solid black lines in Fig. 1(b), the behavior over the evanescent spectrum is very different. Furthermore, the defected array supports a secondary mode that propagates at higher spatial frequencies and is not present in the regular array response [indicated by the dashed lines in Fig. 1(b)]. This mode can be attributed to the appearance of additional coupled resonances introduced by the vacancy defect points inside the structure (similar to how alternating thin layers of positive and negative index media can support coupled surface waves at layer interfaces [26]). As a result, we would expect that the bound modes within a

defective array slab would not resemble those of the regular array lens and may not even be evanescent inside the slab. It has been shown elsewhere, however, that similar bound modes in a multilayered slab can amplify evanescent waves over a wider spatial frequency and thus have improved resolution over a solid negative-index slab of the same thickness [10, 27–29]. In Sec. III C, we directly solve for the bound modes of a slab of the defected array metamaterial and analyze the slab response to incident waves in order to investigate our hypothesis of improved imaging through the introduction of point defects.

III. BOUND MODES IN INFINITE MD METAMATERIAL SLABS

In this section, we analyze the bound modes guided along infinitely wide slabs as the physical origins of evanescent wave amplification. In Sec. III A, we begin by studying guided bound modes along an infinite slab of an ideal homogeneous double-negative medium to give insights into how they contribute to perfect imaging. Then we use numerical solutions of the wave equation for an infinite MD-cylinder metamaterial slab to find its bound modes and estimate its transmission response over the evanescent spectrum. In Sec. III B, we study the bound modes guided along an infinite slab of the regular array MD metamaterial. In Sec. III C, we analyze the bound modes for an infinite slab of the defected array metamaterial and discuss the effects of introducing vacancy points. In both sections we present bound mode dispersion diagrams and full-wave simulations of transmission at the operating frequency ω_o.

A. Ideal homogeneous double-negative slab

Using the analytic eigenmode solutions for a slab of dispersive material [5], the dispersion diagrams of bound modes guided along Veselago slabs embedded in air with thickness $d = a = 0.0642\lambda_o$ and $5a = 0.321\lambda_o$ are shown in Fig. 2. These bound modes arise from symmetric and antisymmetric coupling of surface-plasmon polaritons at the two interfaces of the infinite slab. As can be seen in this figure, the flat dispersion line of an uncoupled single interface (dotted line) has been split into two curves with resonance frequencies above ω_o for even surface bound modes and below ω_o for odd surface bound modes. These dispersion curves asymptotically approach the operating frequency (indicated by the solid red line) as k_x increases, approaching faster for thicker slabs where the coupling between surface-plasmon polaritons is weaker. The ideal Veselago lens always operates between the even and odd mode resonance frequencies, exciting each mode precisely in such a way as to provide unity transmission across a source-to-image-plane distance of $2d$ [5].

As shown by the flat dash-dotted red line in Fig. 2, a slight change in the operating frequency (which slightly distorts the ideal material parameters) causes the bound mode dispersion curve to intersect with the operating frequency, introducing a resonance that prohibits perfect imaging. These intersection points are indicated by red dots in the dispersion diagram. It is also apparent that the imaging performance would be further degraded for a thicker slab since the intersecting resonance point appears at a lower spatial frequency.

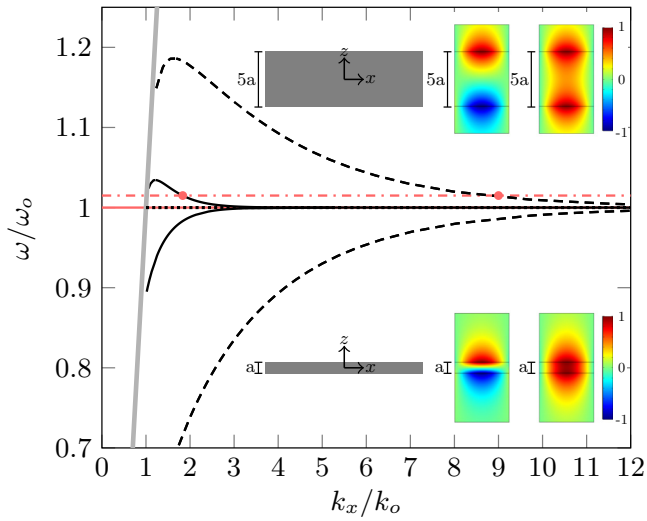

FIG. 2. Dispersion diagrams of even bound modes (upper lines) and odd bound modes (lower lines) guided along ideal homogeneous double-negative slabs of thickness a (dashed black lines) and $5a$ (solid black lines). The geometry of the slabs and the magnetic field distributions (H_y) of even and odd bound modes are plotted in the inset diagrams. The field plots correspond to a wave vector $k_x = 1.7k_o$. The light line is indicated by the solid gray line. The dispersion diagram of uncoupled surface-plasmon polariton waves at a single interface is shown by the flat dotted black line at ω_o. The flat solid red line indicates the operating frequency ω_o in which both values of ε and μ are equal to -1. The flat dash-dotted red line corresponds to a slight deviation in operating frequency from ω_o and the subsequent appearance of bound modes at the intersection points indicated by the red dots.

The magnetic field distributions of odd and even surface bound modes under TM polarization are shown in the inset of Fig. 2 for $k_x = 1.7k_o$. These field plots illustrate how evanescent wave growth within a Veselago slab can be interpreted as the superposition of even and odd bound modes with destructive interference at the front face and constructive interference at the back face.

B. Regular array metamaterial slab

In this section, we study the resonant bound modes guided along an infinitely long slab of the regular array MD metamaterial embedded in air. We solve for the eigenmodes of a single unit cell of the slab as a function of transverse wave vector k_x. Figure 3(c) shows the schematic diagram of the simulation setup for a five-layer slab in which periodic boundary conditions are assigned to the top and bottom sides and perfectly matched layers (PMLs) are placed at the left and right sides of the domain. The height of the domain is equal to the slab periodicity a and the width is set large enough for the evanescent tails of the slab bound modes to be negligibly small at the PML interfaces (ensuring a real valued eigenfrequency).

Figure 3(a) shows the frequency dispersion diagram of guided bound modes along a monolayer slab and a five-layer slab plotted over the first Brillouin zone (BZ). An incident evanescent wave can be amplified by coupling to the slab

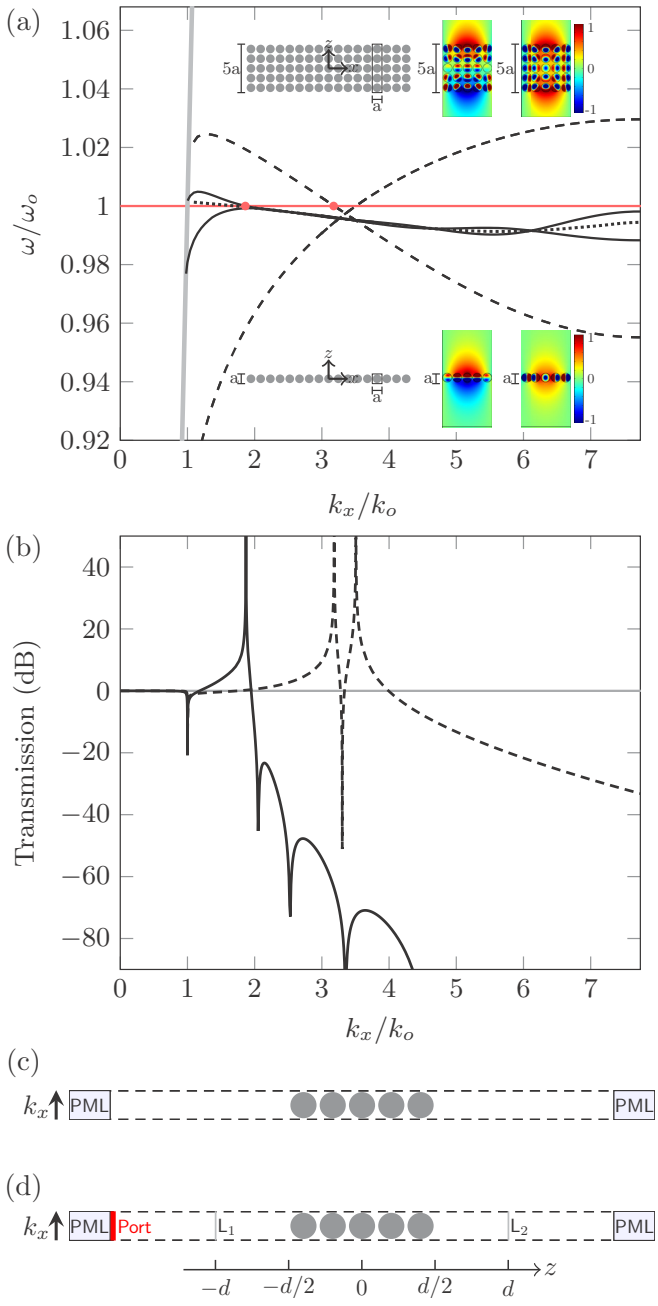

FIG. 3. (a) Dispersion diagrams of guided bound modes along infinite slabs of the regular array MD metamaterial and (b) the transfer function of the slabs at ω_o. The results for a monolayer MD slab and a five-layer MD slab are shown by the dashed black lines and solid black lines over the first Brillouin zone (up to $|k_x| = \pi/a = 7.73k_o$), respectively. The even bound modes (corresponding to the upper lines at low spatial frequencies) intersect with ω_o to produce a transmission peak at $k_x = 1.871k_o$ for the five-layer and at $k_x = 3.183k_o$ for the monolayer slab. The slab geometries, unit cells, and bound mode field distributions corresponding to $k_x = 1.7k_o$ are plotted in the inset diagrams. The dispersion diagram of uncoupled single interface surface waves is shown in (a) by the dotted black line. The ideal transfer function of Veselago slabs is shown in (b) by the flat gray line at 0 dB. Diagrams of the simulation setups used to generate the dispersion diagram and transmission response of the infinite regular array slab are shown in (c) and (d), respectively.

mode with the corresponding transverse wave vector. For example, consider the magnetic field distribution of even and odd modes plotted as insets in Fig. 3(a). These modes resemble coupled surface modes within the Veselago slab and can similarly amplify incident evanescent waves. As can be seen from the dispersion curves of the monolayer slab (dashed black line) and the five-layer slab (solid black line), however, they can mimic the ideal lens behavior only until the dispersion curves of the even modes intersect with the flat line at ω_o (the even modes provide the lowest spatial frequency intersections). These intersection points are indicated by red dots in the dispersion diagrams. As the thickness of the slab increases, the curves appear closer to the dispersion line of uncoupled surface modes guided along a single interface (shown by the dotted line and calculated using a very thick slab where the coupling between the surface modes at each interface is negligible). This pushes the intersection point with ω_o to lower spatial frequencies, thereby reducing the spatial bandwidth of the lens. For example, the first resonance of the five-layer slab at the operating frequency occurs for the even bound mode at $k_x = 1.871k_o$.

To quantify the response of the metamaterial slabs to propagating and evanescent waves at ω_o, we use full-wave simulations to calculate the transfer function for plane waves transmitted from the source plane ($z = -d$) to the image plane ($z = d$) as a function of transverse spatial frequency k_x. We use the simulation setup shown in Fig. 3(d) and solve for the transmitted field given an incident plane wave with a transverse wave vector k_x. In this setup, the dashed lines represent periodic boundary conditions, the incident wave is generated through a simulation port (shown in red), and PMLs are used to terminate the scattered waves. The transmission is then calculated as the ratio of the transmitted Fourier coefficient at the image plane (L_2) to the incident Fourier coefficient at the source plane (L_1) using

$$T = \frac{\int_{L_2} H_t(x,z)e^{-ik_x x}dx}{\int_{L_1} H_i(x,z)e^{-ik_x x}dx}, \tag{3}$$

where $H_i(x,z)$ is the incident magnetic field and $H_t(x,z)$ is the transmitted magnetic field.

Figure 3(b) plots the amplitude of the total transmission function for a monolayer slab (dashed black line) and a five-layer slab (solid black line) alongside the ideal transmission of a Veselago slab (flat gray line). The response of the metamaterial slabs to propagating waves is similar to the Veselago slab over the propagating spectrum, with nearly uniform 0-dB transmission. However, the metamaterial slabs only mimic the ideal lens behavior over the evanescent spectrum below the transmission resonances (indicated by the peaks in the response). These peaks correspond to the points where the dispersion curves intersect with ω_o, and cause the imaging performance of the metamaterial slab to be restricted in the following two ways. First, the amplification of evanescent waves is dramatically reduced after the appearance of resonances, placing an upper spatial frequency limit to the evanescent components of an object that can be reconstructed in the image plane. In other words, the resonance peaks limit the minimum focal spot diameter corresponding to the image

of an illuminating point source. Second, the overamplification of the object components at or near the resonances manifests as high-intensity lobes which obscure the image of the object.

C. Defected array metamaterial slab

In this section, we solve for the bound modes guided along an infinite slab of the defected array metamaterial and analyze the slab response to incident waves using the methods described in the previous section [see Figs. 4(c) and 4(d) for diagrams of the simulation setups]. We study a defected array slab of thickness $5a$ and compare it to the response of the five-layer regular array metamaterial slab. The dispersion diagram of bound modes over the first BZ of the defected array slab (up to $|k_x| = \pi/2a = 3.89k_o$) and the geometry of the defected array metamaterial are shown in Fig. 4(a). Note that unlike the homogeneous double-negative medium and the regular array metamaterial higher-spatial frequency propagating modes are present in the defected array [shown by the dashed lines in Fig. 1(b)] that prevents surface modes from forming at a single interface. This fundamentally changes how the bound modes are formed since they do not arise from the simple coupling between the surface modes of the slab. As can be seen in this figure, the defected array slab can guide odd bound modes with a flat dispersion profile near ω_o and an intersection point pushed up to $k_x = 2.824k_o$. The near-resonant coupling of incident evanescent waves at ω_o to these odd bound modes provides amplification over a wide range of the evanescent spectrum that results in higher spatial resolution imaging [11]. The transfer function of the defected array slab at ω_o is shown in Fig. 4(b) in order to quantitatively demonstrate the response of the slab to an incident wave. The defected array slab has a nearly unity transfer function over the propagating spectrum and provides amplification for higher spatial frequencies up to the first resonance peak [coinciding with the first intersection point in Fig. 4(a)].

We can gain insights into the operation of the defected array slab by considering the bound modes of multilayered MD slabs composed of either longitudinally stacked transverse monolayers spaced with air (wherein each layer is parallel to the x axis) or transversely stacked longitudinal monolayers spaced with air (wherein each layer is parallel to the z axis). Note that a single MD monolayer guides bound modes along the layer [see Fig. 3(a)] and a multilayered stack of MD monolayers forms a coupled-waveguide structure with similar properties to the anisotropic multilayered stack of alternating thin layers of positive and negative index media [26]. First, we consider the slab composed of transverse monolayers. This corresponds to introducing air gaps (i.e., line vacancy defects) parallel to the slab interfaces between each layer of MD cylinders. The dispersion diagram of bound modes in this structure approaches the diagram of a single monolayer MD slab in Fig. 3 with the resonance pushed to higher spatial frequencies. Below the resonance point, however, these modes are far from ω_o and cannot provide the amplification of the regular array MD slab. This is not unexpected, given the evanescent decay across each of the air gaps between layers. Second, we consider the slab composed of longitudinal monolayers. This corresponds to introducing air gaps (line vacancy defects) that are perpendicular to the slab interfaces. These monolayers

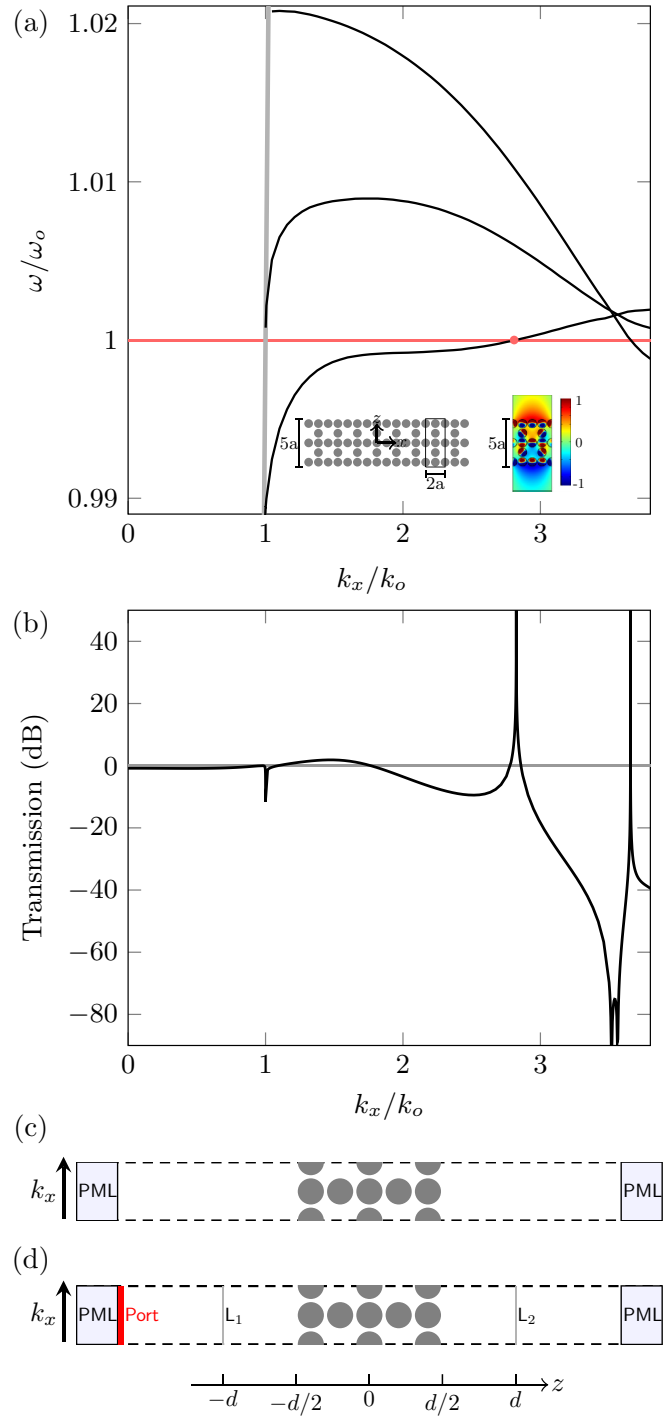

FIG. 4. (a) The dispersion diagrams of guided bound modes along the defected array metamaterial slab and (b) the transfer function of the slab at ω_o over the first BZ (up to $|k_x| = \pi/2a = 3.98k_o$). The middle curve in (a) represents an even bound mode while the upper and lower curves represent odd bound modes. The odd bound mode corresponding to the lowest line at low spatial frequencies intersects with ω_o to produce the first transmission peak at $k_x = 2.824k_o$. The MD slab geometry and unit cell are plotted in the inset diagrams alongside the magnetic field distribution of this guided odd mode at $k_x = 1.7k_o$. Diagrams of the simulation setups used to generate the dispersion curves and transmission response of the infinite defected array slab are shown in (c) and (d), respectively.

act as transmission lines, allowing the slab to sustain bound modes with relatively flat dispersion near ω_o. The horizontal monolayers couple poorly to incident waves, however, and the overall amplification of the slab is minimal. Although both structures shift the resonant slab modes to higher spatial frequencies, evanescent waves are not strongly amplified and propagating waves can only be focused if the source and image planes are nearly adjacent to the slab interfaces. The proposed defected array slab, however, combines both layered structures, providing high coupling and amplification over a wide range of the evanescent spectrum, while mimicking the focusing mechanism of a perfect lens over the propagating spectrum.

IV. RESONANT MODES IN FINITE MD METAMATERIAL LENSES

In this section, we use full-wave eigenmode simulations to study the resonant modes and imaging artifacts of a MD metamaterial lens with finite transverse width. As discussed in previous sections, bound modes guided along an infinite slab at the operating frequency (identified by the red dots at the dispersion diagram intersection points) appear as high-intensity lobes which obscure the image of the object. Here, we consider a finite width for the lens which reduces the continuous dispersion curves of infinitely long slabs to discrete resonances in ω-k space. These resonant modes can have symmetric or antisymmetric field distributions in the transverse and longitudinal directions (across the $x=0$ and $z=0$ planes, respectively). Due to scattering from the top and bottom edges of the lens, these modes are generally not completely bounded, resulting in a complex resonant frequency $\omega_r + i\gamma$, where γ is a damping term that accounts for radiation loss. In the following section we study the dominant resonant modes (at or very close to the operating frequency) in the regular and defected array lenses of finite width.

A. Regular array metamaterial lens

As discussed in Sec. III B, the bound mode guided by an infinite five-layer regular array slab at ω_o has longitudinal even symmetry and a low transverse wave vector $k_x = 1.871k_o$. Not surprisingly, the dominant resonant modes within a finite regular lens also have even symmetry along the z axis [see Figs. 5(a) and 5(b)], resulting in nondirective scattering from the edges of the lens. These radiated fields are weakly confined to the lateral side of the lens and appear as side lobes across the image plane. The low spatial frequency components of the resonant modes make them easy to excite, resulting in strong imaging artifacts. For example, a regular array five-layer lens with width $65a$ (not shown for the sake of brevity) has a resonant mode at the operating frequency ($\omega_r = \omega_o$ and $\gamma/\omega_o = 6.3437 \times 10^{-5}$). When this lens is used for imaging, the mode is strongly excited at its resonance and completely obscures the object image.

By carefully choosing the lens width, the resonance frequency of the dominant modes can be detuned from the operating frequency to reduce the mode amplitudes; however, this mitigation is limited. For example, a regular five-layer lens with width $59a$ does not have a resonant mode at ω_o

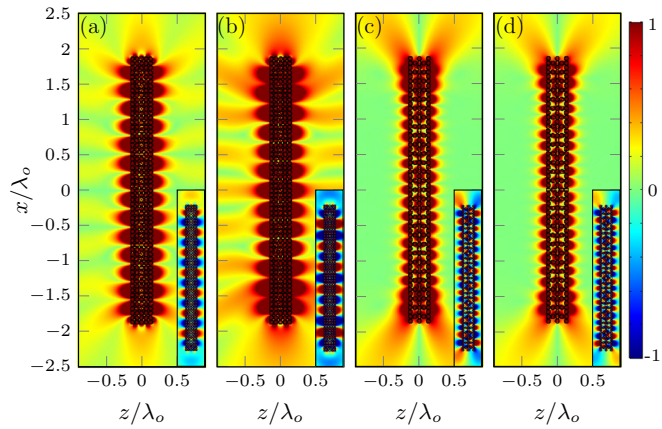

FIG. 5. Magnetic field intensity plots of the dominant resonant modes for the MD metamaterial lenses of width $59a$ and thickness $5a$. The resonance modes of the regular array lens are plotted in (a) and (b) and have an even longitudinal symmetry (along the z axis). (a) The resonant mode with $\omega_r = 0.9998\omega_o$ and $\gamma/\omega_o = 4.3085 \times 10^{-5}$ has transverse odd symmetry (along the x axis). (b) The resonant mode with $\omega_r = 1.0003\omega_o$ and $\gamma/\omega_o = 1.1288 \times 10^{-4}$ has transverse even symmetry. The defected lens resonant mode plots in (c) and (d) have an odd longitudinal symmetry. (c) The resonant mode with $\omega_r = 0.9998\omega_o$ and $\gamma/\omega_o = 5.8441 \times 10^{-5}$ has transverse even symmetry. (d) The resonant mode with $\omega_r = \omega_o$ and $\gamma/\omega_o = 4.1274 \times 10^{-5}$ has transverse odd symmetry. The inset diagrams plot the real part of the field to show the transverse and longitudinal symmetries of each mode.

[see Figs. 5(a) and 5(b)]; however, the off-resonance mode fields are not well confined to the lens and can lead to strong imaging artifacts. The robustness of this lens in imaging different objects will be studied further in Sec. V.

Taking the Fourier transform of the magnetic field over the surface of the lens at $z = 2.5a$ shows that resonant mode fields in Figs. 5(a) and 5(b) have dominant transverse spatial variations equal to $k_x = 1.93k_o$ and $1.82k_o$, respectively. These have similar spatial frequencies to the even bound mode of the infinite slab at the operating frequency [i.e., they are located near the first red dot in Fig. 3(a) at $k_x = 1.871k_o$], which demonstrates consistency between the dispersion of the infinite and finite slab modes. Furthermore, far from the lenses, the field patterns exhibit low spatial variations with transverse wavenumbers near k_o. This can be attributed to the fact that the slabs can also support an even bound mode near the light line just above ω_o [see the solid line in Fig. 3(a)].

B. Defected array metamaterial lens

As discussed in Sec. III C, the first resonant mode guided by the defected array slab at ω_o [identified by the red dot in Fig. 4(a)] is an odd mode with a transverse wave vector $k_x = 2.824k_o$ (this is higher than that of the regular array slab). The dominant resonant modes within a finite defected array lens have the same odd symmetry along the z axis as the infinite slab. As can be seen in Figs. 5(c) and 5(d) for a lens of width $59a$, the odd symmetry produces scattering at the edges of the lens that is directed away from the image plane. The resonant mode fields are therefore confined closer to the lens

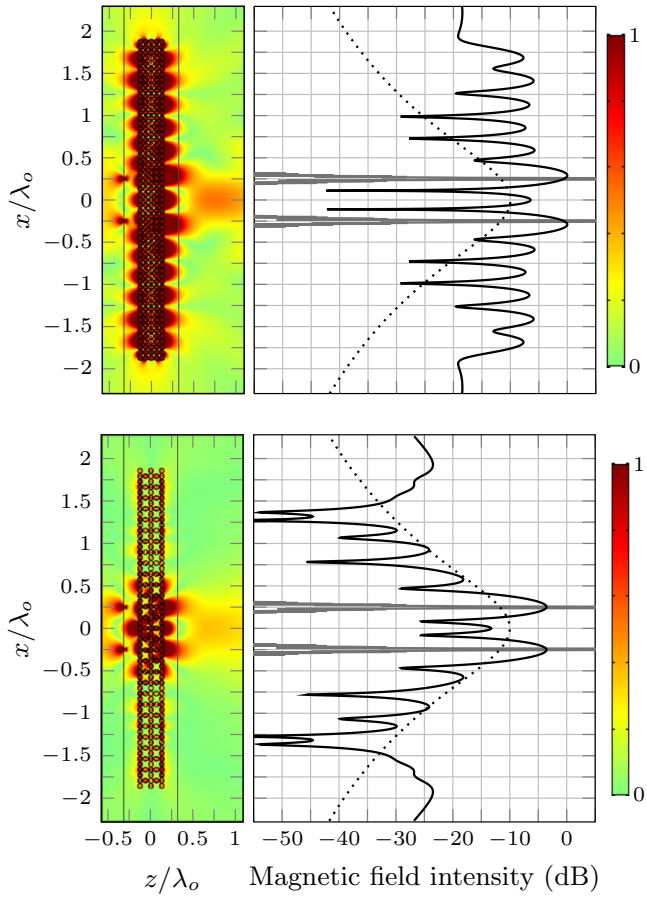

FIG. 6. Imaging field plots for the regular array lens (top) and the defected array lens (bottom). Each lens has thickness $5a$, has width $59a$, and is illuminated by two x-polarized electric dipoles located at $x = 0.25\lambda_o$ and $-0.25\lambda_o$. The magnetic field intensity is plotted over the xz plane on the left, while the normalized field intensity at the image plane is plotted on the right in solid black. The image field without the lens is plotted in dotted black, along with the source plane field intensity of the object in solid gray. The source plane at $z = -5a$ and the image plane at $z = 5a$ are indicated by thin black lines in the field plots.

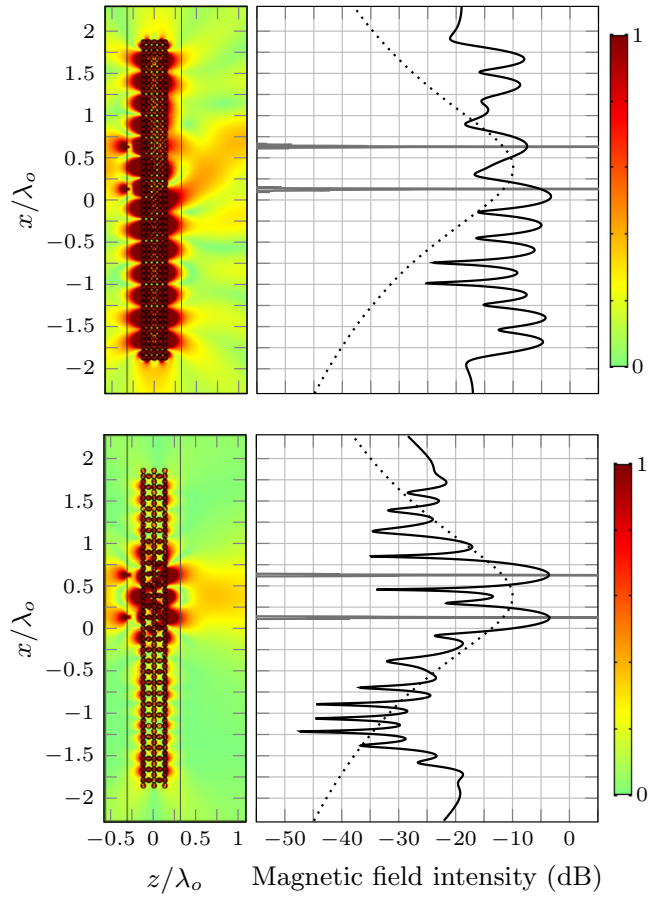

FIG. 7. Field plots similar to the ones shown in Fig. 6 for two offset electric dipoles located at $x = 0.13\lambda_o$ and $0.63\lambda_o$.

surface with amplitudes that are suppressed by this radiation loss. The higher spatial frequency of the resonances also results in weaker excitation by the highly decaying evanescent components of the object field. Compared to the regular array lens, we see a significant decrease in imaging artifacts in the defected array lens. Simulation results show that although the defected array lens has a resonant mode at the operating frequency [see Fig. 5(d)] the mode fields do not extend into the image plane. This means that compared to the regular array lens the performance of the defected array lens is less sensitive to the location of resonances and is more robust to the transverse width. The resonant mode fields shown in Figs. 5(c) and 5(d) have dominant transverse spatial variations equal to $k_x = 2.68k_o$ and $2.82k_o$, respectively, which occur near the spatial frequency of the odd bound mode of the infinite slab at the operating frequency [indicated by the red dot at $k_x = 2.824k_o$ in Fig. 4(a)]. Unlike the regular array lens, the field patterns of the defected array lens do not exhibit the same low spatial variations far from the lens because the lens does not support odd bound modes near the light line close to ω_o [see Fig. 4(a)]. In the next section, we demonstrate and quantify the improvements in imaging performance of the defected array lens over the regular array lens.

V. IMAGING PERFORMANCE OF FINITE MD METAMATERIAL LENSES

In this section, we study the imaging performance of the regular array lens and the defected array lens using full-wave simulations. The object to be imaged consists of multiple two-dimensional electric dipoles with moments aligned parallel to the x axis. Each dipole emits a transverse magnetic field H_y with a uniform source-plane Fourier spectrum across both propagating and evanescent domains. This enables the response of each lens to be studied across a broad spatial bandwidth. Figures 6–8 compare the imaging performance of the regular array lens (shown in the top of the figure) and the defected array lens (shown in the bottom of the figure) given various object configurations. Both lenses have a thickness of $5a$, have a width of $59a$, and are centered at the origin. The source and image planes are separated by a distance equal to twice the lens thickness and are located at $z = -5a$ and $5a$, respectively. In these figures, the field plots on the left show the magnetic field intensity distribution over the xz plane, while the plots on the right show the normalized

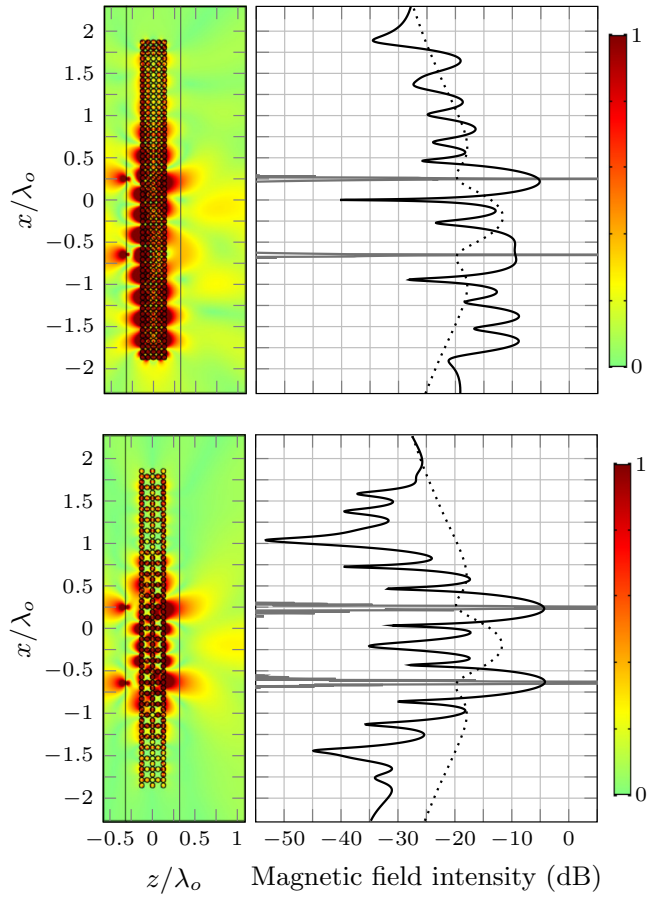

FIG. 8. Field plots similar to the ones shown in Fig. 6 for two offset electric dipoles with wider spacing located at $x = 0.25\lambda_o$ and $-0.65\lambda_o$.

transverse field intensity in decibels ($20 \log |H_y|$) at the image plane. The field intensity at the source and image planes for empty space without the lenses are also plotted for reference. All the intensity plots in this section are normalized with respect to the maximum value of the image intensity for the regular array lens in Fig. 6. This provides a quantitative comparison of the performance of each lens across different object distributions.

Figure 6 illustrates that both the regular array lens and the defected array lens produce two distinct peaks at the image plane for a pair of symmetrically centered dipole sources separated by $0.5\lambda_o$. The image from the defected array lens, however, is much clearer with lower side lobe levels and more distinct peaks. The image peaks of the regular array lens are also laterally shifted from the true object positions. These imaging discrepancies reflect the differences between the excited resonant modes within the regular and defected array lenses and the differences between the resulting imaging artifacts.

We now investigate the robustness of these lenses to object configurations which are not symmetrically centered on the lens. Figure 7 plots the image fields for the same two dipoles offset by $0.28\lambda_o$ along the x axis. As shown in the top figure, the superposition of the object image with the resonant mode excited within the regular array lens produces an image in which the locations of both sources are no longer identifiable.

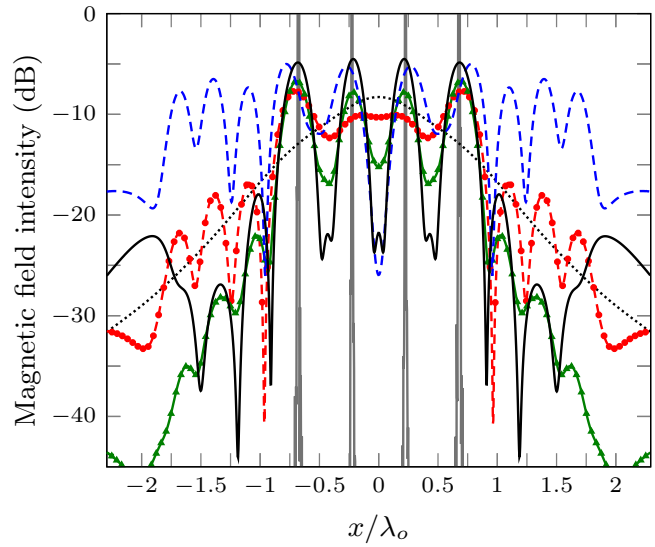

FIG. 9. The normalized field intensity at the image plane for imaging with lossless and lossy MD lenses. The illuminating sources are four x-polarized electric dipoles located at $x = 0.675\lambda_o$, $0.225\lambda_o$, $-0.225\lambda_o$, and $-0.675\lambda_o$. The fields from the lossless regular and defected array lenses are plotted in dashed blue and solid black lines, respectively. The fields from the regular and defected array lenses with lossy inclusions (with electric and magnetic loss tangents equal to 10^{-3}) are plotted in dashed red with circle markers and solid green with triangle markers, respectively. The normalized source field intensity of the object and image intensity without the lens are plotted in solid gray and dotted black, respectively.

By contrast, as shown in the bottom figure, the defected array lens has no trouble resolving and locating the object dipoles. This implies that the resolution of the objects observed in Fig. 6(a) may simply have been a consequence of the object spectrum matching the spectrum of a resonance mode within the regular lens. When the spectra are mismatched, however, as in Fig. 7(a), the objects are no longer resolved.

In Fig. 8, the sources are separated further to a distance of $0.9\lambda_o$ and offset by $0.2\lambda_o$. Despite the larger separation distance, the regular array lens still cannot locate the bottom source at $x = -0.65\lambda_o$ in the image of the lens. The defected array lens has no trouble resolving the object with all side lobes below 13 dB.

Here, we briefly discuss the minimum separation distance necessary to resolve symmetric dipoles. We first consider a pair of centered dipoles (as in Fig. 6) and use the Rayleigh criterion to define the image resolution as the minimum distance between two point sources that results in a drop of 0.91 dB between their image peaks. Simulation results (not shown here for brevity) demonstrate that a pair of dipoles is still resolvable when the separation between them is reduced to $0.3192\lambda_o$ and $0.2951\lambda_o$ for the regular array lens and the defected array lens, respectively. We then consider an object composed of four evenly spaced dipoles symmetrically centered over the source plane. The four dipoles provide a more complex source to test the imaging resolution under more robust conditions. Our simulation results (again, not shown here for brevity) demonstrate that in order to resolve the object the separation between the dipoles should be increased to $0.4286\lambda_o$ for the

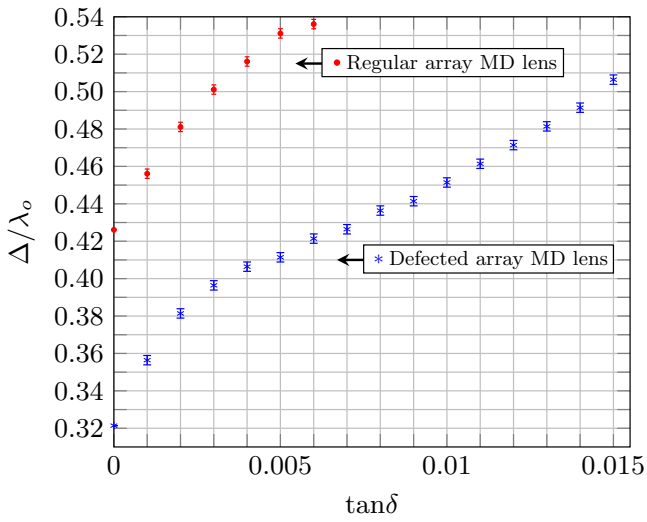

FIG. 10. The minimum separation distance (Δ) necessary to resolve four symmetric dipoles in the image of the regular array lens (red circle markers) and the defected array lens (blue asterisk markers) as a function of the electric and magnetic loss tangent of the MD inclusions (tanδ). The length of error bars is equal to $0.005\lambda_o$.

regular array lens and to $0.3239\lambda_o$ for the defected array lens. These results further confirm that the effect of resonant modes should not be ignored in analyzing the imaging performance and that resolving a pair of symmetric point sources does not provide a sufficiently rigorous test for super-resolution.

We now investigate the effect of material loss on the imaging performance of the regular array lens and the defected array lens. Figure 9 plots the image field intensity corresponding to an object composed of four symmetric dipoles separated by $0.45\lambda_o$. Two cases are considered: in the first, the lenses are composed of lossless MD cylinders ($\varepsilon = \mu = 20$), while, in the second, low loss cylinders are used in which the electric and magnetic loss tangents are equal to 10^{-3} ($\varepsilon = \mu = 20 + 0.02i$). In the absence of loss, both the regular array lens and the defected array lens generate images that can resolve the point sources, although the image produced by the regular array lens has prominent side lobes and peaks that are laterally shifted from the true object positions (due to interference with the resonant mode fields). In the presence of absorption, the resonance modes are suppressed in the regular array lens; however, the spatial resolution is also reduced and the lens can no longer resolve the inner point objects. By contrast, the defected array lens can still resolve all four objects.

We systematically investigated the imaging resolution of the regular array lens and the defected array lens by gradually varying levels of material loss. Figure 10 plots the minimum separation distance (Δ) necessary to resolve four symmetric dipoles as the electric and magnetic loss tangent (tanδ) of the MD inclusions is varied. The plot shows that a lossy defected array lens with $\tan\delta < 0.006$ has a higher resolution than the lossless regular lens. While the regular array lens can resolve sources separated by a distance $\Delta = 0.5\lambda_o$ for $\tan\delta < 0.003$, the same resolution can be achieved by the defected array lens for much higher loss $\tan\delta < 0.014$ (which is within the range reported for low loss magnetodielectric materials [30]). This demonstrates the improved imaging robustness of the defected array lens and the importance of designing superlenses with resonance modes in mind.

VI. CONCLUSION

In this paper, we have investigated the impact of resonant modes on the imaging performance of a negative-index metamaterial lens. We showed that although a metamaterial lens can mimic the response of a perfect lens over the propagating spectrum the evanescent response can differ significantly. The excitation of resonant modes within the lens limits the spatial frequency bandwidth and introduces imaging artifacts that degrade the imaging fidelity and robustness. Furthermore, we show that the standard two-source resolution test can be unreliable when applied to superlenses. In particular, some demonstrations of super-resolution arise simply as a consequence of the object spectrum matching the spectrum of the dominant resonant mode. For example, we show that a regular array of MD cylinders can image a pair of illuminating point sources when symmetrically centered in front of the lens but not when that symmetry is broken. Achieving robust imaging performance therefore requires an understanding of how resonant modes produce artifacts and requires that all super-resolution claims are supported by comprehensive resolution testing.

We showed that the resolution and robustness of a metamaterial lens can be improved by tailoring its resonant modes to avoid artifacts. Using the MD cylindrical metamaterial as an example, we introduced defects into the array to push the resonant modes to high spatial frequencies and direct the edge-scattered fields away from the image plane. We show that these defects also mitigate the effects of material losses on subwavelength resolution. This paper provides deeper insight into the behavior of resonant modes and their effects on imaging and provides a comprehensive method to study super-resolution imaging in metamaterial lenses. These methods can now be applied to other two- or three-dimensional metamaterial structures in order to improve the imaging performance and ensure robustness—important steps towards the ultimate goal of designing a practical superlens.

ACKNOWLEDGMENTS

This work was supported by the Natural Sciences and Engineering Research Council of Canada through the Discovery Grant program. The authors would also like to acknowledge CMC Microsystems for the provision of CAD tools that facilitated this research.

[1] M. Born and E. Wolf, *Principles of Optics* (Cambridge University, Cambridge, England, 1999).

[2] J. B. Pendry, Phys. Rev. Lett. **85**, 3966 (2000).

[3] V. G. Veselago, Soviet Phys. Usp. **10**, 509 (1968).

[4] X. S. Rao and C. K. Ong, Phys. Rev. B **68**, 113103 (2003).
[5] R. E. Collin, Prog. Electromagn. Res. **19**, 233 (2010).
[6] R. Ruppin, Phys. Lett. A **277**, 61 (2000).
[7] R. Ruppin, J. Phys.: Condens. Matter **13**, 1811 (2001).
[8] L. Solymar and E. Shamonina, *Waves in Metamaterials* (Oxford University, New York, 2009).
[9] S. A. Shakir and A. F. Turner, Appl. Phys. A **29**, 151 (1982).
[10] E. Shamonina, V. A. Kalinin, K. H. Ringhofer, and L. Solymar, Electron. Lett. **37**, 1243 (2001).
[11] C. Luo, S. G. Johnson, J. D. Joannopoulos, and J. B. Pendry, Phys. Rev. B **68**, 045115 (2003).
[12] P. A. Belov, C. R. Simovski, and P. Ikonen, Phys. Rev. B **71**, 193105 (2005).
[13] M. J. Freire and R. Marqués, Appl. Phys. Lett. **86**, 182505 (2005).
[14] R. A. Shelby, D. R. Smith, and S. Schultz, Science **292**, 77 (2001).
[15] A. N. Lagarkov and V. N. Kissel, Phys. Rev. Lett. **92**, 077401 (2004).
[16] G. Shvets and Y. A. Urzhumov, Phys. Rev. Lett. **93**, 243902 (2004).
[17] C. L. Holloway, E. F. Kuester, J. Baker-Jarvis, and P. Kabos, IEEE Trans. Antennas Propag. **51**, 2596 (2003).
[18] X.-X. Liu and A. Alù, Metamaterials **5**, 56 (2011).
[19] R. A. Shore and A. D. Yaghjian, Radio Sci. **42**, 1 (2007).
[20] A. Alù, Phys. Rev. B **84**, 075153 (2011).
[21] L. Markley, Phys. Rev. B **94**, 085108 (2016).
[22] I. Aghanejad and L. Markley, Phys. Rev. B **96**, 205157 (2017).
[23] X.-X. Liu and A. Alù, J. Nanophotonics **5**, 053509 (2011).
[24] http://www.comsol.com.
[25] C. Fietz, Y. Urzhumov, and G. Shvets, Opt. Express **19**, 19027 (2011).
[26] S. Feng, J. M. Elson, and P. L. Overfelt, Opt. Express **13**, 4113 (2005).
[27] J. Pendry and S. Ramakrishna, Physica B: Condens. Matter **338**, 329 (2003).
[28] S. A. Ramakrishna, J. B. Pendry, M. C. K. Wiltshire, and W. J. Stewart, J. Mod. Opt. **50**, 1419 (2003).
[29] N. Mattiucci, G. D'Aguanno, M. Scalora, M. J. Bloemer, and C. Sibilia, Opt. Express **17**, 17517 (2009).
[30] H. Su, X. Tang, H. Zhang, Y. Jing, and F. Bai, J. Electron. Mater. **43**, 299 (2014).